Oregon Undergraduate Research Journal
8.1 (2015) ISSN: 2160-617X
ourj.uoregon.edu

Rotational Properties of the Extraordinary Multi-tailed Asteroid P/2013 P5

Annika Gustafsson, Physics and Math*

ABSTRACT

Observations made with the Hubble Space Telescope in September 2013 revealed that the asteroid known as P/2013 P5 appeared to have six comet-like tails. Jewitt et al. (2013) concluded that this extraordinary structure and activity could not be explained by traditional near-surface ice sublimation or collision events ejecting particles from the asteroid's surface. Instead, the most likely explanation is that this unusual object has been spun-up by solar radiation forces to a critical limit which has resulted in the rotational disruption of the asteroid causing the unique six-tail structure. This interpretation predicts that the nucleus of this comet-like asteroid should be in rapid rotation. In November 2013, broadband photometry of P/2013 P5 was obtained with Lowell Observatory's 4.3-meter Discovery Channel Telescope using the Large Monolithic Imager to investigate the possibility of rapid rotation. While the variation in the rotational light curve from these data was too small to be justifiable, morphological changes in the nucleus-coma system were observed.

1. INTRODUCTION

To date, there are twelve known celestial bodies in the Solar System, labeled Main Belt Comets (e.g. Hsieh & Jewitt, 2006) or Active Asteroids (Jewitt, 2012). These are objects that exhibit both asteroid and comet-like properties, typically with a circular, asteroid-like orbit and a comet-like dust tail. Among them is P/2013 P5, a comet-asteroid transition object discovered by the PAN-STARRS telescope in August 2013. Jewitt et al. (2013) further investigated this object in September 2013 with the Hubble Space Telescope (HST). The high-resolution camera revealed the unique six comet-like dust tails of asteroid P/2013 P5 (Figure 1). Jewitt et al. (2013) observed the object on both September 10, 2013 and September 23, 2013. In this two-week time span between observations, P/2013 P5 displayed many differences in the appearance of its six tails. Tail A changed the least in length and brightness, while Tail F increased in both length and brightness. By performing a comet tail modeling technique called synchrone modeling, Jewitt et al. (2013) used a range of particle sizes and positions to conclude that each tail of P/2013 P5 was the result of an individual event. From the synchrone modeling, they determined that the first tail (Tail A) originated April 15 ± 2 days and the sixth tail (Tail F) originated on September 4 just days before Jewitt et al. (2013) observed the asteroid on September 10, 2013. With tail activity evident over a

*Annika Gustafsson is a senior physics and math major in the Robert D. Clark Honors College from Santa Cruz, California. When not studying for classes or working, you can find her teaching group fitness classes at the UO Recreation Center or watching her favorite sports teams. She was also a member of the 2012 Acrobatics and Tumbling National Championship Team. Annika's academic interests lie in astronomy and physics and she hopes to receive her PhD in Astrophysics or Planetary Science with the intentions of pursuing a career in observational research. Please direct all correspondence to agustafsson@gmail.com.

five-month period between April and September, the object has sustained consistent mass loss, and therefore, exhibits a comet-like appearance. The unique six-tail feature makes asteroid P/2013 P5 of particular interest to the study of asteroid-comet transition objects.

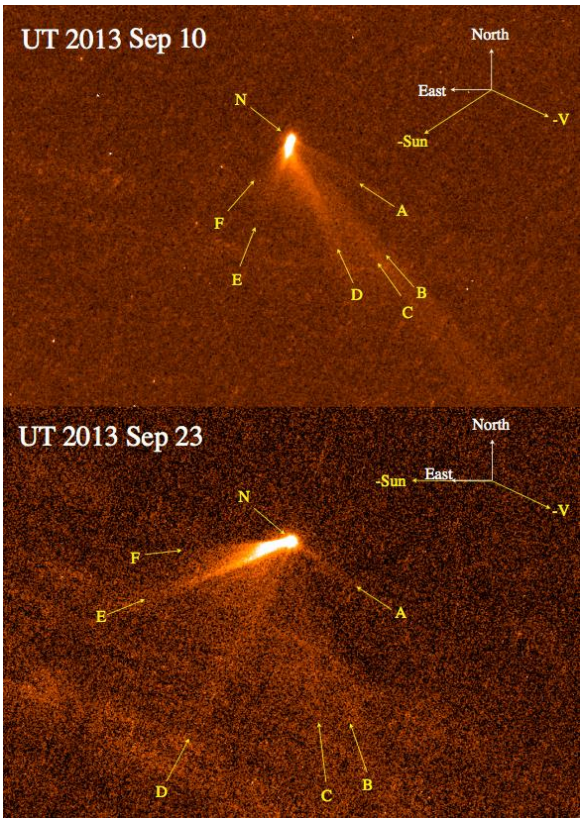

Figure 1: Hubble Space Telescope Image of P/2013 P5 taken on September 10, 2013 (top) and September 23, 2013 (bottom). The appearance of the object changes between the images with its six unique tails (A-F) growing both in length and brightness from the top image to the bottom image. The width of the image is 23,000 km, equivalent to 28 arcseconds (28") in astronomical units, with the tails extending approximately 25" (Jewitt et al., 2013).

2. PURPOSE

The purpose of this research is to study the unique comet-like properties of asteroid P/2013 P5 and to search for a mechanism to explain such activity for an object that is traditionally inactive. Data were taken by Dr. Stephen Levine at the Discovery Channel Telescope (DCT) in November 2013 using the Large Monolithic Imager (LMI). The findings will contribute to the field of active-asteroid research by furthering the understanding of the evolution and possible disruption mechanisms of asteroids. As a result, this research will also ultimately advance our understanding of the formation and evolution of the Solar System because asteroids are direct remnants of the formation.

3. BACKGROUND

3.1 PLANET FORMATION

Current hypotheses about the origins of the Solar System suggest that our sun formed from an over-dense molecular cloud which collapsed approximately 4.56 billion years ago. Once a molecular cloud collapses, it becomes the birthplace for stars. Through conservation of angular momentum, the cloud of gas and dust surrounding the new star flattens and becomes an accreting disk called a protoplanetary disk. Over time, the protoplanetary disk loses its gas cloud and becomes a debris disk composed of dust grains that may combine to form small celestial bodies called planetesimals. Some of these planetesimals merge and continue to accrete material to form planets, while other planetesimals that do not accrete enough dust or do not fuse together with another planetesimal, form asteroids and other small bodies in the Solar System. These planetesimals now occupy the Asteroid Belt, Kuiper Belt, and Oort Cloud (Figure 2).

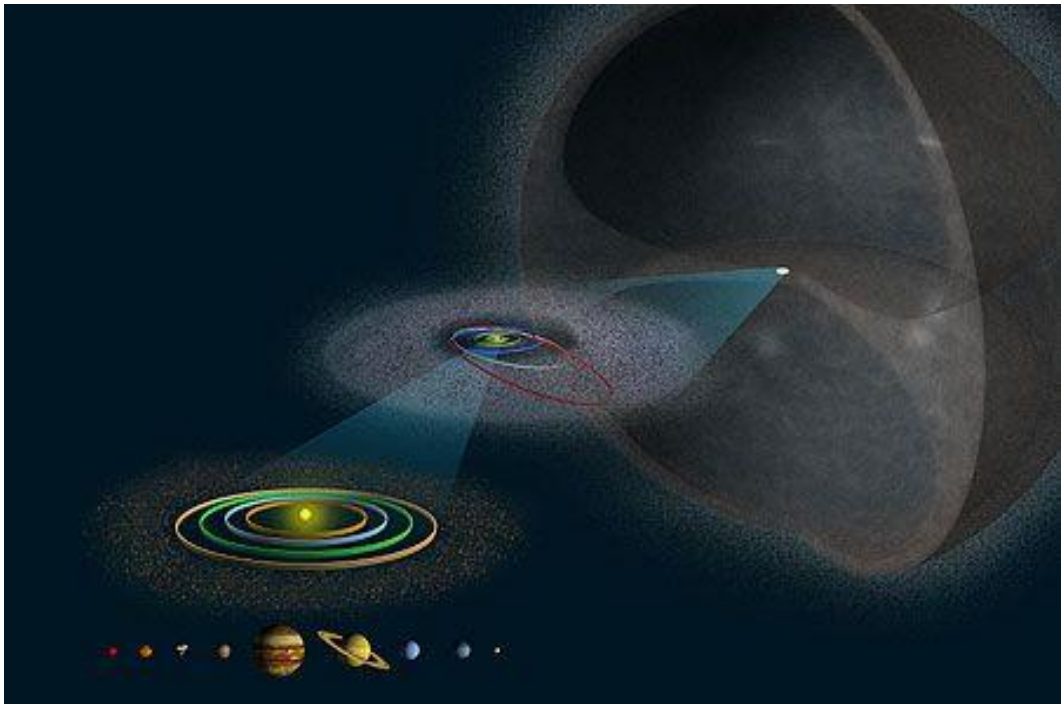

Figure 2: The Asteroid Belt (left) resides between Mars and Jupiter in the inner solar system. The Kuiper Belt (center), which lies just beyond Neptune, is home to many short period comets. The Oort Cloud (right) is mysterious in that it is predicted to be a giant cloud outside of the planets surrounding the sun. It houses icy objects with less regular orbits, longer periods, and higher eccentricity, or ellipticity, than objects in the Asteroid Belt and Kuiper Belt.

3.2 SMALL BODIES

Small bodies consist of asteroids, comets, Oort Cloud objects, Kuiper Belt objects, and small planetary satellites in the Solar System. These bodies are classified as outer and inner small Solar System bodies based on their distance from the Sun. Objects beyond Neptune are referred to as outer small Solar System bodies and consist of comets, Kuiper Belt objects, and Oort Cloud objects. The inner small Solar System bodies, falling within the orbit of Neptune, consist of Main Belt asteroids and Jupiter Trojans.

Comets and asteroids are identified based on both their physical and dynamical properties. Physically, comets are icy bodies that reside in the outer solar system, typically in the Kuiper Belt and Oort Cloud. Comets are often icy because they were formed beyond the "snow-line", an imaginary line in the solar system that separates the terrestrial planets from the gas and ice giants. As a result, comets contain a large amount of volatile material. Hsieh et al. (2004) states that observationally, comets have a gravitationally unbound atmosphere called a coma and an accompanying tail, while asteroids do not. This is usually the result of near-surface ice sublimation where the comet is turned on and off as it goes through perihelion and aphelion, closest approach to the sun and furthest approach from the sun. As volatiles sublimate from the surface, gas and dust from the comet's interior are excavated and ejected due to the very low surface gravity of a typical cometary nucleus. Because asteroids contain much less volatile material, these physical properties are not usually observed. Asteroids and comets also have very different orbital properties. While comets have highly elliptical orbits, asteroids have much more circular orbits (Figure 3). This distinction is quantified using a parameter called the Tisserand parameter (T_J)

$$T_J = \frac{a_J}{a} + 2\left[(1-e^2)\frac{a}{a_J}\right]^{1/2}\cos(i). \quad (1)$$

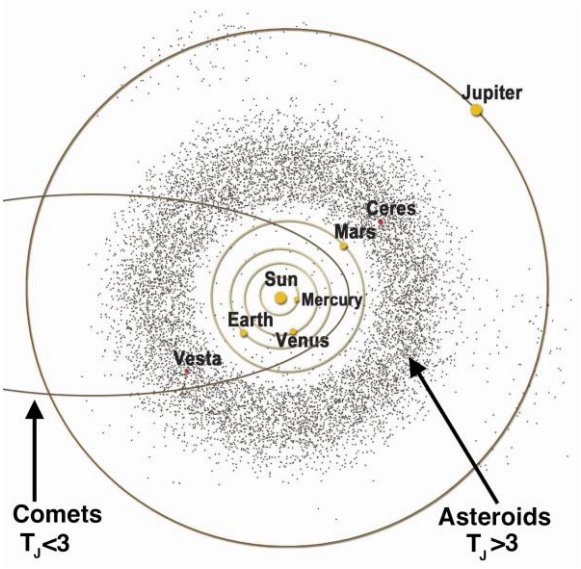

Figure 3: Comets and asteroids have very different dynamical properties. Comets have highly elliptical orbits quantified by a $T_J<3$ while asteroids have more circular orbits with a $T_J>3$.

The Tisserand parameter is a measure of small body orbital elements including semi-major axis (a), inclination (i), and eccentricity (e) of a small body and a larger perturbing body (a_J), which, for comets and asteroids, is Jupiter (Eq.1). Most comets have a $T_J<3$, while asteroids have a $T_J>3$. P/2013 P5 has a T_J of 3.66 (Jewitt et al., 2013), placing it in the category of asteroids ($T_J>3$) due to its asteroid-like orbit.

Below, Figure 4 shows nine of the eleven active asteroids that have been discovered as of March 2012 (Jewitt, 2012). All of these objects, including P/2013 P5, resemble comets in their appearance, making the asteroid-comet categorization more complex.

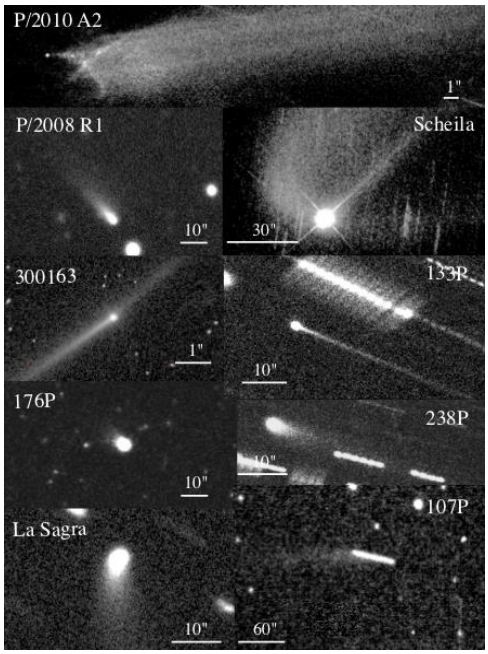

Figure 4: Eleven active asteroids have been discovered since 2004 including the nine shown above where the tail can be spatially resolved (Jewitt 2012).

3.3 ACTIVE ASTEROIDS

It was not until after the discovery of 133P/Elst Pizarro (Figure 5) in 1996 that astronomers began focusing on the comet-asteroid transition and studying objects that fell into a categorical grey area. Elst Pizarro was the first asteroid discovered with comet-like activity. When it was initially studied in 1996, the tail was deemed the result of a chance impact, and thereby predicted to extinguish. However, this conclusion was disproved when the comet-like activity was observed again by Hsieh et al. in 2004. Hsieh et al. (2004) studied the asteroid for several months and observed changes in the structure and brightness of the dust tail. As a result, they concluded that the tail was not the product of a one-time impact, but instead that it was actively generated over long periods of time revealing that the asteroid was in fact losing mass. The cause of the mass loss, however, was unclear.

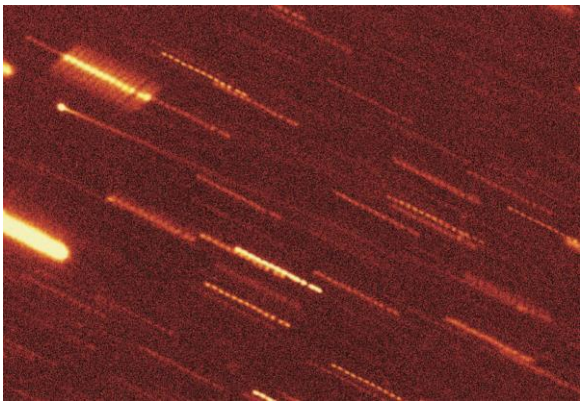

Figure 5: Elst Pizarro (upper left corner) was the first active asteroid discovered in 1996. The activity was eventually deemed the cause of near-surface ice sublimation by Hsieh et al. (2004).

3.4 REASONS FOR MASS LOSS

Mass-losing asteroids are now referred to as Main Belt Comets or Active Asteroids. Historically, near-Earth asteroids (NEAs) were studied as possible extinct or dormant comets. Hartmann, Tholen, and Cruikshank (1987) described the different stages of a comet: active, dormant, and extinct. They discussed the possibility that some comets may be misidentified as asteroids in appearance due to a very faint tail or coma that is not observable from earth. This ambiguity became a popular area of research because astronomers were interested in determining if any NEAs were at risk of becoming active again. On the other hand, the concept of asteroids having a comet-like appearance was puzzling to astronomers who were unsure of how an asteroid, with a limited amount of volatile material, would begin to generate mass loss.

Jewitt (2012) describes the eleven current explanations for how asteroids can lose mass. These explanations fall under three main processes related to collisional events, near-surface ice sublimation, and rotational fission. While collision events and near-surface ice sublimation are conceptually simple explanations, rotational fission is more complicated and less understood.

The Classical Model for asteroids describes their evolution based on collisions and gravitational effects, but is unable to explain the origin of NEAs (Bottke, 2006). Non-gravitational forces, first discussed by Yarkovsky in the early 1900s, can help to reconcile this issue (Bottke, 2006). These non-gravitational forces are referred to as the Yarkovsky and YORP Effects (Figure 6).

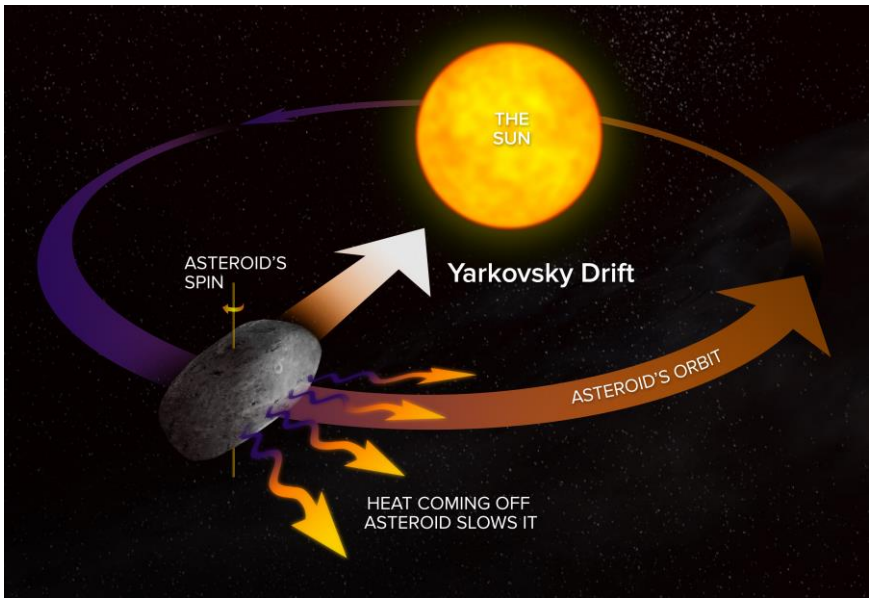

Figure 6: Solar radiation forces, known as the Yarkovsky and YORP Effects, heat up the sunward side of small bodies and alter both the orbit and rotation rate of the objects (Figure from NRAO).

As the object orbits around the sun, the sunward side of the object warms up and the heat is ultimately re-radiated into space. Since photons carry momentum, the asteroid feels a net force opposite in direction to that in which thermal photons are emitted from the hottest point on the surface. Since the object has thermal inertia, resulting in a temperature distribution delay, the object also feels a force along the direction of its orbit. This force results in an increase or decrease in the semi-major axis of the object's orbit depending on the direction of rotation- prograde or retrograde motion. This is referred to as the Yarkovsky Effect. While the Yarkovsky Effect alters the orbit, the YORP effect alters the spin rate. The reflection and re-emission of sunlight creates a net thermal torque on the object as a result of the non-uniformity of its shape, causing the object to either spin up or spin down. The Yarkovsky Effect is the result of rotation, whereas the YORP Effect is due to both rotation and shape. An object that is perfectly spherical will not undergo the YORP torque. Most small bodies, however, are very irregularly shaped. Because of this, they experience the Yarkovsky and YORP Effects simultaneously. Once an asteroid has been spun up by the YORP Effect, it is susceptible to rotational fission, or breakup.

There are two leading theories to explain the process of rotational fission. Scheeres (2007) looks at the different outcomes for a contact binary system that has been spun up by the YORP effect (Figure 7). Scheeres (2007) describes a macroscopic process where rotational fission occurs when the angular momentum of the object has been increased to the point where centripetal acceleration overcomes gravitational binding so that the bodies are no longer in contact.

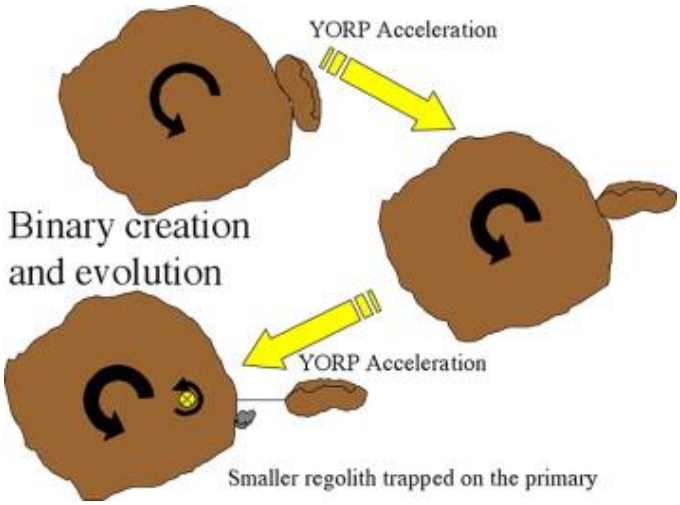

Figure 7: Contact binary asteroids will fission once spun up to the critical spin rate as a result of Yarkovsky and YORP effects (Scheeres 2007).

Walsh (2008) instead looks at how a small binary asteroid system is formed when a rubble pile asteroid is spun up to the critical spin limit by YORP torques. As the rotation of the asteroid increases, self-gravity and centrifugal forces due to the rotation cause stress, allowing mass to leave the poles and accumulate near the equator. The object bulges and mass is shed from the equator, which allows the asteroid to reach a minimum energy state (Figure 8). The shed material can then accrete to form satellites.

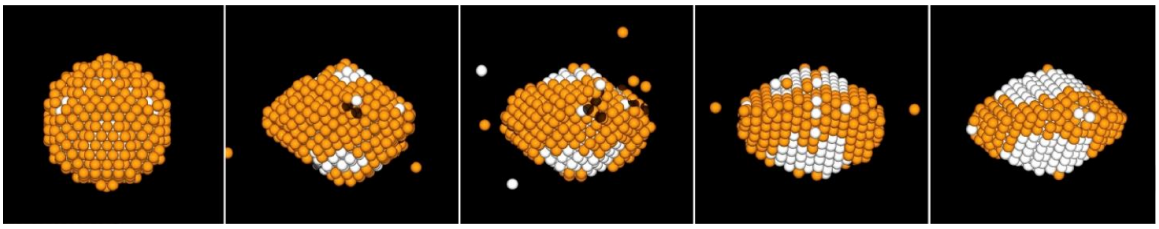

Figure 8: With enough angular momentum, rubble pile asteroids will rotationally fission by shedding mass in the equatorial plane to form satellites (Walsh 2008).

4. HYPOTHESIS

P/2013 P5 is an inner belt asteroid with a semi-major axis of 2.189 Astronomical Units (AU). Jewitt et al. (2013) predicted P/2013 P5 to be a member of the Flora asteroid family based on its location in the inner belt. Due to the history of the Flora family and the small size of the P/2013 P5, which is just under 0.5 km in diameter, P/2013 P5 is thought to have likely undergone many collisions in its lifetime. As a result, the asteroid probably contains little to no volatile material,

making it highly unlikely that the cause of activity is a product of near-surface ice sublimation. As noted previously, Jewitt et al. (2013) took data of P/2013 P5 on both September 10 and September 23. A summary of their results is shown below in Table 1. On each night, a multi-tailed structure was observed extending further than 25". While the nucleus remained in tact, the brightness and position of the tails changed between the nights, leading Jewitt et al. (2013) to conclude that each tail is the result of a separate event. It is extremely unlikely that this asteroid has undergone six separate collision events in a five-month period. As a result, collision is an unlikely cause of activity. Jewitt et al. (2013) claimed that the most likely explanation for the cause of the six unique tails in P/2013 P5 is spin-up and rapid rotation of the asteroid by the solar radiation forces and torques of the YORP Effects. My research plan is to further investigate Jewitt's hypothesis that the cause of activity is due to rapid rotation of the nucleus of P/2013 P5.

Table 1: Summary of Jewitt et al. (2013) results.

Name	Value
Semi-major Axis	2.189 AU
Eccentricity	0.115
Inclination	5°.0
Nucleus	$< 0.24 \pm 0.04$ km
T_J	3.66
H_v	18.6
p_v	0.29 ± 0.09

5. OBSERVATIONS

P/2013 P5 was observed on Universal Time (UT) 2013 November 18 using the Large Monolithic Imager instrument on the 4-meter Discovery Channel Telescope. A summary of the observations is detailed in Table 2 located at the end of this paper. The Large Monolithic Imager is an all-purpose charged coupled device (CCD) camera that images a large 12.5x12.5 arcminute field of view. The data images were binned 2x2 pixels providing a higher spatial resolution of 0.24"/pixel instead of 0.12"/pixel, allowing for the tails of P/2013 P5 to be resolved in the images. At the time of the observations, P/2013 P5 was at a heliocentric distance of 2.028 AU, a geocentric distance of 1.553 AU, and a predicted magnitude of 21.0. The direct scale comparison of my Discovery Channel Telescope data to Jewitt et al.'s Hubble Space Telescope data is shown in Figure 9 below.

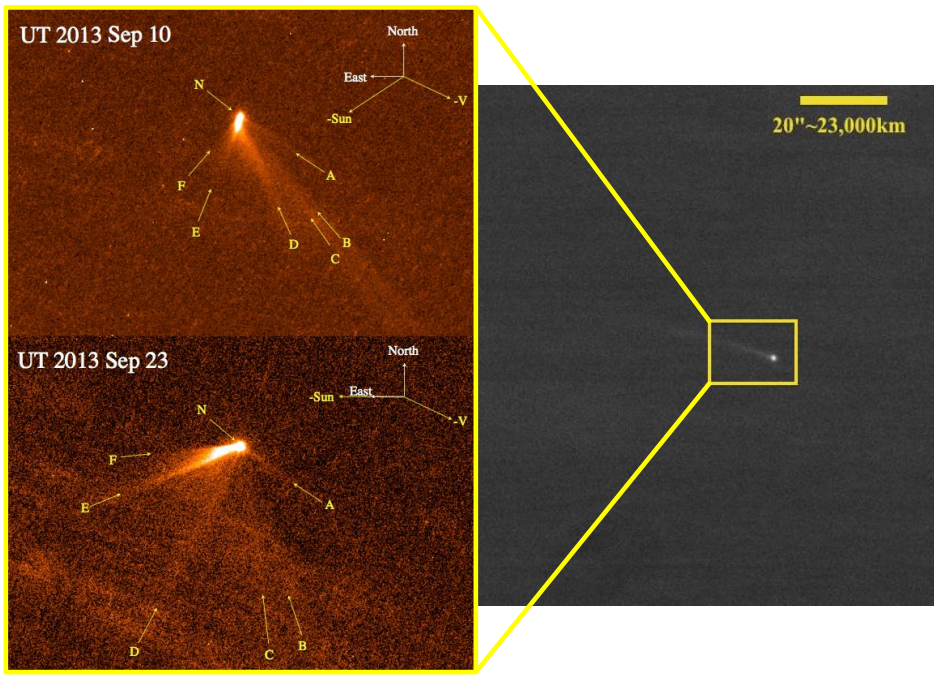

Figure 9: Scale comparison of HST image versus DCT image of P/2013 P5 (Jewitt et al. 2013). DCT image of P/2013 P5 created from composite of asteroid-rate tracked images. The tail extends >20". The width of the image is 2' (135,000 km).

6. METHODS

6.1 DATA REDUCTION

The programming languages Interactive Data Language (IDL) and Image Reduction and Analysis Facility (IRAF) were used to reduce and analyze the data to arrive at the proposed conclusions about the rapid rotational period of the nucleus of P/2013 P5. The reduction is a multi-step process that includes three different types of data files: biases, flat fields, and science data.

The bias images and overscan regions are used to calculate the zero noise level of the charged coupled device (CCD) camera. The zero noise level is a pixel intensity offset that is inherent to the CCD, so that once calculated, the offset is subtracted off of all of the asteroid data images. This bias offset is used to avoid negative intensities in the CCD readout when taking data. There are two ways to evaluate the bias offset- through bias images or an overscan region. Bias images are zero second exposures taken with the shutter closed to have data on the readout of unexposed pixels. The overscan region is a set of rows and columns that are added to each data image. These are not physical rows or columns, but instead pseudo rows and pseudo columns created by scanning additional cycles to the readout. The bias frames are usually more useful than the overscan regions because they represent a 2D bias image where the bias offset can be subtracted pixel by pixel from each image, while the overscan is only a 1D vector.

The second type of CCD data file, flat field, is used in a correction process of the CCD detector. CCDs are not perfect imaging devices. Within the CCD, each pixel responds differently to the light coming in. Therefore, it has a different Quantum Efficiency value when compared to its neighboring pixels. The purpose of a flat field image is to correct for this inconsistency. The goal is to have a flat field that consists of uniform illumination of every pixel by a light source that has an identical response to that of the science data. By dividing by a normalized flat field, the pixel-to-pixel variations are removed. There are two types of flat fields: dome flats and twilight flats. Dome flats are taken using a uniformly illuminated screen on the inside wall of the dome whereas twilight flats are taken on a blank piece of sky. While flat fields are primarily used to correct for the pixel-to-pixel variations, they are also used to correct for dust donuts that appear on the image frames as a result of dust on the filters or primary mirror. Flat fields at the Discovery Channel Telescope were created using Twilight Flats.

The third type of CCD data file, science data, is unique to each research goal. For this project, the science data consists of about forty images taken over the course of four hours using the LMI detector at the DCT in Flagstaff, Arizona. All data frames were taken using the Sloan Digital Sky Survey (SDSS) r' filter. The first four images were tracked on the stars using sidereal tracking, while the remaining images were non-sidereal tracked, and instead, tracked on the asteroid.

All of the data files described above were used together to reduce the science data using both IDL and IRAF software. The method for reducing data in IDL is a much more interactive process, while IRAF has many procedures pre-written for convenience. Both software programs require the same reduction steps. The major steps include accounting for instrument effects by subtracting off the bias file and removal of atmospheric effects by applying a flat field correction. These standard reduction steps were performed on all asteroid data files in both IRAF and IDL languages.

After reducing the data, the stacked image shown in Figure 9 above was created as a composite of all asteroid-rate tracked images that were combined to increase the signal-to-noise ratio of P/2013 P5. The increased resolution of the stacked image shows an extended tail from the nucleus greater than 20", slightly less than the size of the tail Jewitt et al. (2013) observed using HST.

6.2 PHOTOMETRY

To prove that the cause of activity on P/2013 P5 is rotational fission resulting from the YORP Effect, we investigated the rotational period of the nucleus using photometry. Astronomical photometry is a technique involving the calculation of total flux of the target object. Once the flux is calculated, the measurement can be converted to an absolute magnitude and plotted with time as a light curve. Here, the rotational period can be calculated. If the object is in fact undergoing a rapid rotation, we would expect to see a light curve with a period of 2.2 hours.

To begin the photometry process, differential photometry and magnitude calibration were performed at the same time for each image. Differential photometry observes both the target object (P/2013 P5) and the comparison objects (solar analog field stars) at the same time in the same image. Solar analog field stars have the same colors as that of our Sun. The sunlight that is

reflected off of objects like comets and asteroids is the light that is collected by the telescope, so comets and asteroids appear solar colored.

Photometric calibration was executed on the magnitude of five solar analog field stars in both the sidereal and non-sidereal rate tracked images. The solar colors are defined as the difference in magnitude between two consecutive filters. The DCT data were taken using the Sloan Digital Sky Survey (SDSS) r' filter. In the Sloan field, the filters used are *ugriz*. Solar colors are therefore defined as the difference in magnitude for *u-g*, *g-r*, *r-i*, and *i-z* magnitudes. The Aladin interactive sky atlas from Strasbourg Astronomical Data Center was used with the SDSS-DR9 (Release 8 2012) catalog to search for solar analog field stars that were also in my field of view. Once solar analogs with a range of magnitudes were found, the Aladin software was used to determine the absolute magnitude of the solar analog field stars. Because we are looking at only solar-colored objects, the standard photometric equation can be reduced and simplified (Eq. 2 – Eq. 4).

$$V_{abs} = V_{inst} + Z + \chi \cdot c_1 + (V - R) \cdot c_2 \quad (2)$$

$$V_{abs,asteroid} - V_{abs,star} = V_{inst,asteroid} - V_{inst,star} \quad (3)$$

$$V_{abs,asteroid} = V_{inst,asteroid} - (V_{abs,star} + V_{inst,star}) \quad (4)$$

The standard photometric equation calculates the absolute magnitude of the object (V_{abs}) by applying an offset to the instrumental magnitude (V_{ins}). This offset is composed of a zero point correction (*Z*), an extinction correction (χ), and a color correction (*V-R*). Because the data were only taken using one filter (*r'*), the absolute magnitude of the object can be calculated by using information from the solar analog field stars. By subtracting the photometric equation for P/2013 P5 (Eq. 2) from the photometric equation for a solar analog field star (Eq. 2), the offsets are cancelled out, leaving only the instrumental and absolute magnitudes (Eq. 3). This process allows for the direct calculation of the absolute magnitude of the asteroid by subtracting the magnitude difference of the solar analog field star, "delta-mag", from the instrumental magnitude of the asteroid that is computed by the IRAF *PHOT* package (Eq. 4).

The guidelines explained in *A User's Guide to Stellar CCD Photometry* by Phil Massey were followed to set the photometry parameter values. The basic idea is to place an aperture over the target object and calculate the total flux in the aperture. Initial photometry involving a range of different circular aperture radii and curve-of-growth analysis was used to determine the appropriate aperture radius to use in the photometry of the field stars. From curve-of-growth analysis, a process involving creating plots to maximize the signal-to-noise ratio and maintain 95% of the total flux, an aperture radius of three was selected for the solar analog field stars in the sidereal rate tracked images and an aperture radius of ten was selected for the non-sidereal rate tracked images. Absolute magnitudes specified by the Sloan catalog were used to calculate the calibration offset ("delta-mag") for the transformation from instrumental to absolute magnitude of the asteroid.

Conversely, an aperture radius of ten was selected for the sidereal tracked images and three for the non-sidereal rate tracked images for photometry on the asteroid- reversed apertures from those used for photometry on the field stars. Figure 10 shows the resulting light curve for the asteroid using the stated aperture radii of 10 and 3. The light curve shows both a positive linear trend and some variability. In order to ensure that this variability was unique to the rotation properties of P/2013 P5, photometry using the same procedure was performed on field asteroid 2006 BZ253 that was traveling at a rate of 17"/min, while P/2013 P5 was traveling at 41"/min. Figure 11 shows the light curves of both the 2006 BZ253 and P/2013 P5, revealing similarity between the two. As a result, other sources of variability need to be removed from the data. Because 2006 BZ253 is an asteroid and does not display evidence for mass loss, we would expect that it is rotating with a more standard rotation speed and therefore a shorter period than that of P/2013 P5. Thus, the light curves for these two objects should not look the same.

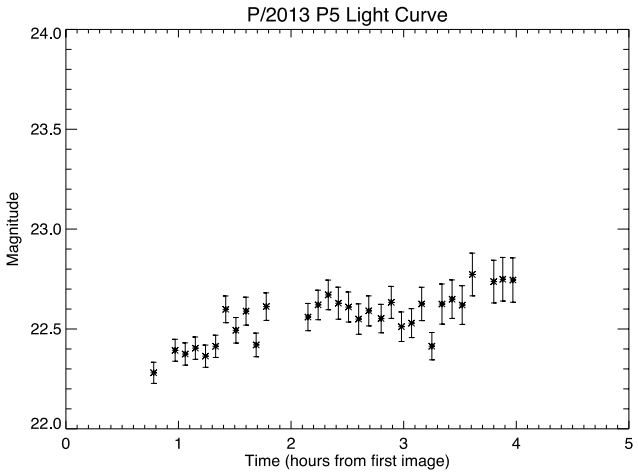

Figure 10: P/2013 P5 Light Curve created using on-chip differential photometry and an aperture radius of 3 pixels.

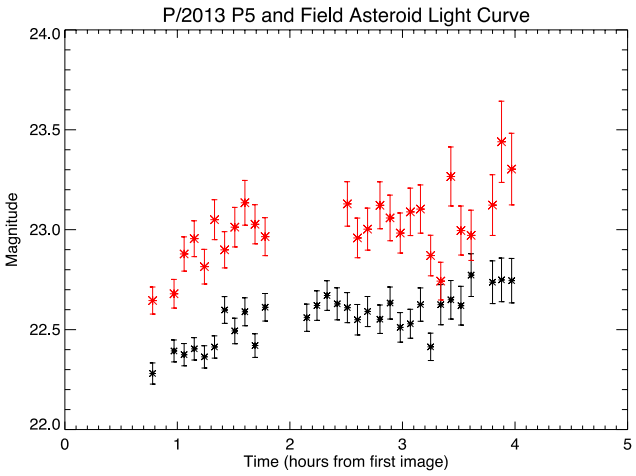

Figure 11: Light curves of P/2013 P5 (black) and 2006 BZ253 (red). Both light curves were created using the same photometric procedures and an aperture radius of 3 pixels.

6.3 CHARACTERIZING VARIABILITY

In order to isolate the rotational properties in the light curve, all sources of variability should be characterized and removed from the data. The first goal was to characterize the effects of seeing. Astronomical seeing describes the blurring and twinkling of astronomical objects caused by the Earth's atmosphere. The easiest way to quantify seeing effects is by calculating the full width at half maximum (FWHM) of the objects. To do this, a cut was taken on the trailed field stars of the asteroid-rate tracked images perpendicular to the direction of the star trails. A Gaussian profile was fit to each cut and the FWHM was plotted with time to quantify the seeing changes throughout the night (Figure 12). This plot illustrates a positive linear trend that is consistent with the linear trend seen in the light curve of P/2013 P5, revealing that the seeing effects had a significant impact on the data.

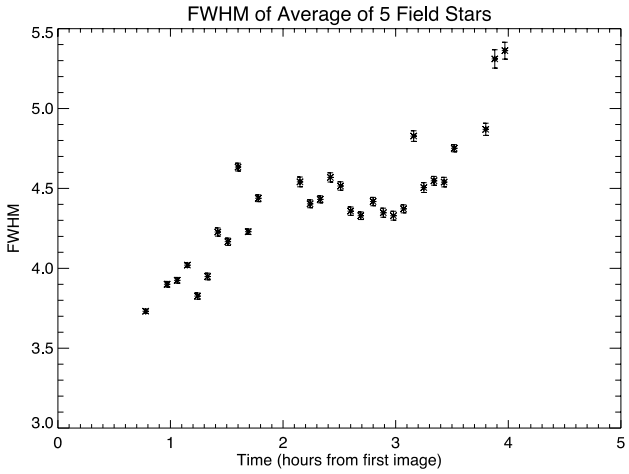

Figure 12: The FWHM was plotted for a Gaussian profile that was fit to field stars in the direction perpendicular to the star trails. The variation in FWHM quantifies the seeing and focus conditions at the time of each image.

The FWHM vector was normalized to an aperture radius of three. This gave a vector of aperture radii that were optimized for the seeing conditions at the time of each image. Scaled aperture photometry was performed on the target asteroid P/2013 P5 using the vector of unique aperture radii specific to each image. Figure 13 shows the resulting light curve for P/2013 P5 using optimized aperture photometry with a variable aperture radius. The plot reveals that the linear trend disappeared with the aperture radius optimization, and there is still some variability in the light curve. The errors are on the level of 0.07 magnitude, while there is no significant variability in the data on the level of 0.15 magnitude.

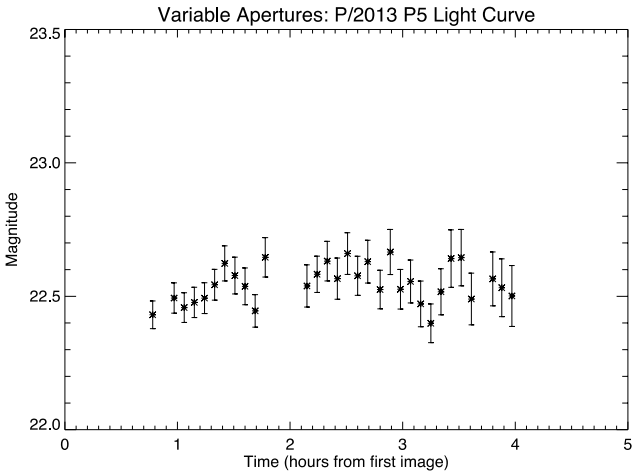

Figure 13: Light Curve of P/2013 P5 created using optimal aperture photometry. Aperture radii were optimized by taking into account the seeing and focus conditions at the time of the image. This was done using the FWHM.

Table 3 located at the end of the paper shows the seeing quantified as a function of both time and airmass. Unfortunately, continuing to characterize the sources of variability would not increase the sensitivity of the variations enough to conclude anything significant about the rotational properties of P/2013 P5. Instead, we chose to proceed forward by analyzing morphological changes in the nucleus-coma of P/2013 P5 instead of through light curves.

6.4 MORPHOLOGY OF P/2013 P5

Looking at changes in the nucleus-coma system in both time and space across the coma relative to the comet's center of brightness could lead to insight in P/2013 P5's rotational properties. We focused on changes in brightness and structure of the coma. The brightness

changes can be observed by looking at how the brightness changes as a function of rotation angle, while the changes in coma are observed by subtracting off the constant nucleus and looking at the changes in the residual. Six stacks of five images were created of asteroid-rate tracked images. These mini stacks were used to track changes in the nucleus-coma system in both time and space.

6.4.1. GENERAL MORPHOLOGY CHANGES

To make an initial inspection of changes occurring in the asteroid, the total flux in the first 90° wedge (the upper left quadrant of the data array) was calculated for each stack and plotted versus time (Figure 14). Figure 14 reveals that there is variation in the flux and the change appears to follow a regular pattern. The variation in the flux is at the level of 10% deviation from the mean. The variation does not fit the trend of seeing throughout the night, which followed a positive linear trend seen in Figure 12, giving us reason to further investigate this variability by looking at both brightness and structure changes in the coma as described above.

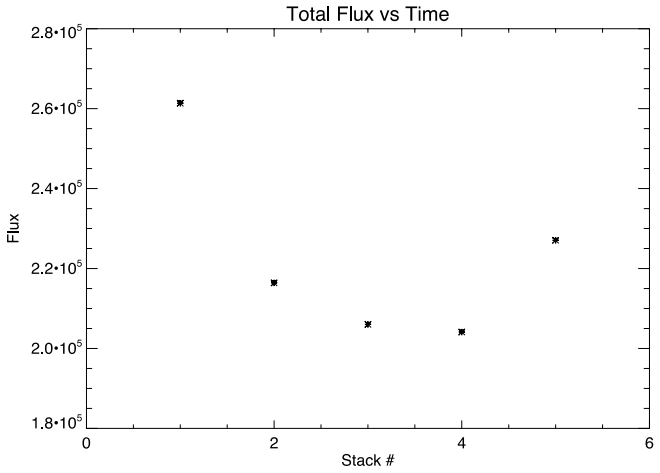

Figure 14: The total flux in a 90° wedge for each of the five mini stacks. The errors are at the level of 0.21% of the mean, while the variance is at the level of 10% of the mean.

6.4.2 BRIGHTNESS CHANGES IN THE NUCLEUS

A 7.68"x7.68" box was extracted from each stacked asteroid image, with the nucleus-coma system located at the center. The box was rotated clockwise in increments of 5°. At each 5° rotation, a 5° wedge was extracted from the box (Figure 15). Larger wedges of 15°, 45°, and 90° were created by summing together the 5° wedges to look for morphological changes (Figure 15).

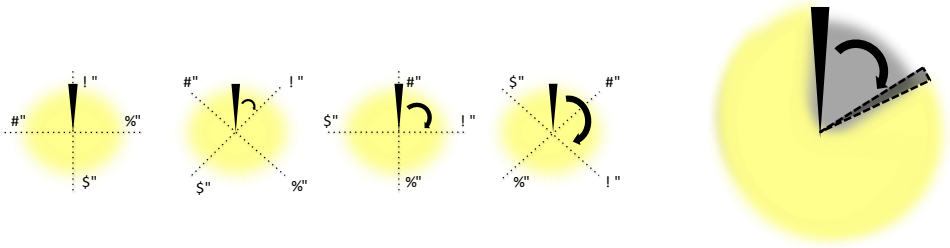

Figure 15: 5° wedges were extracted at every rotation increments of 5° clockwise for each stack. 5° wedges were averaged together to form larger wedges of 15°, 45°, 90°, and 180°.}

Radial profiles of the four 90° wedges for each of the five mini stacked images were plotted, as seen in Figure 16. The brightness of each 90° wedge was tracked between the stacks by taking the total flux of each wedge and ranking its brightness from 1:4 with respect to the other three 90° wedges in the stack. These rankings are displayed in Figure 17 and the values of total flux in each wedge can be seen in Table 4. Each grid in Figure 17 represents an image stack where the colored square symbolizes a 90° wedge in its correct location in the image box. The colors of the squares correspond to the colors in the plots, while the numbers in each square represent the brightness ranking of that 90° wedge. The purpose of Figure 17 was to track wedges as P/2013 P5 rotates throughout the night and determine if there was any pattern to the motion of material in the nucleus-coma system. Based on Figure 17, while there was variation, there were no obvious regular patterns of a peak and trough that were expected if the data gave any insight into the rotational period of P/2013 P5.

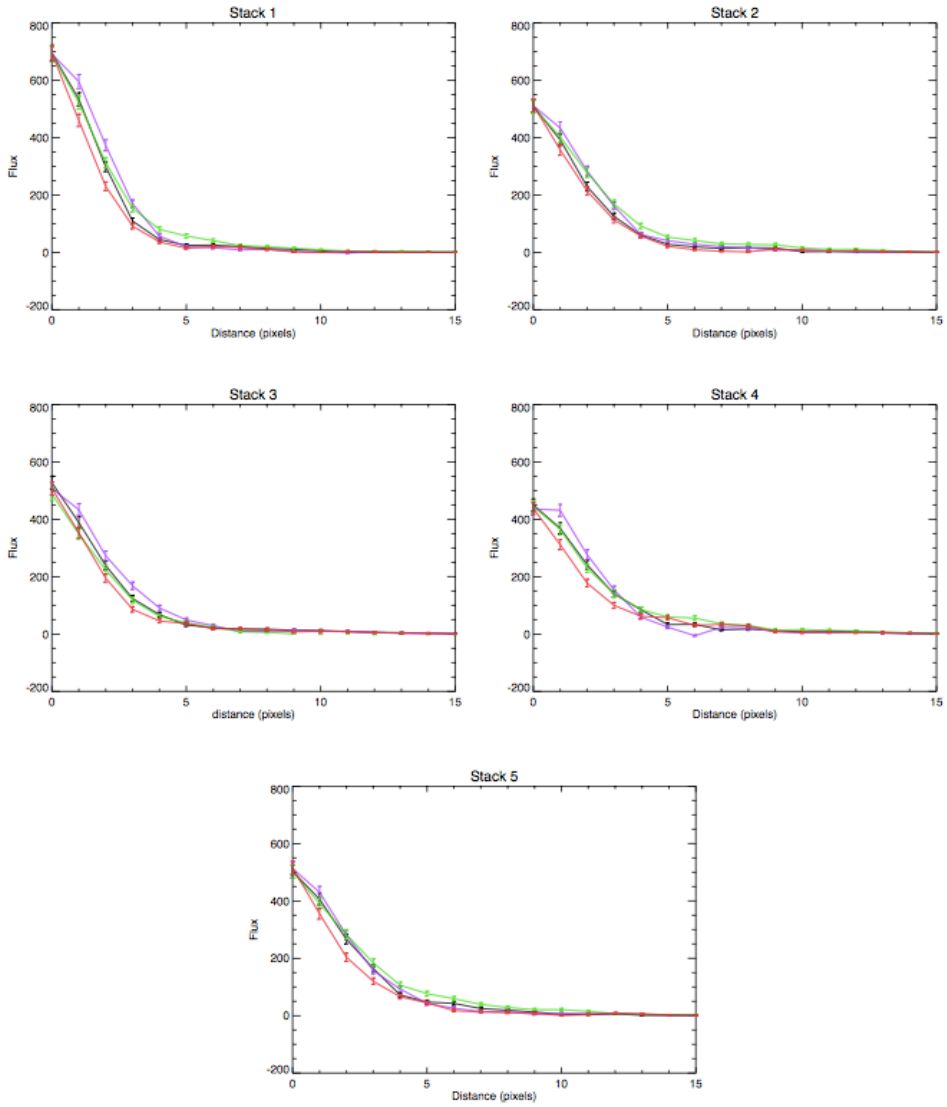

Figure 16: Radial profiles for each 90° wedge for each mini stack. The radial profile goes from the center of P/2013 P5 to the edge of the array, 3.34".

Figure 17: Brightness ranked from 1:4 using total flux in the 90° wedge. (Brightest=1, Least Bright=4.)

Table 4: The total flux of each 90° wedge for each mini-stack.

Wedge #	Flux
1901	1783.09
1902	1948.73
1903	1942.88
1904	1585.64
2901	1422.52
2902	1588.18
2903	1675.82
2904	1324.74
3901	1482.07
3902	1614.69
3903	1313.70
3904	1312.83
4901	1429.00
4902	1454.13
4903	1514.57
4904	1272.03
5901	1575.93
5902	1607.04
5903	1744.70
5904	1379.62

6.4.3 CHANGES IN THE COMA

While the brightness changes in the nucleus revealed variations, again, no clear pattern was observed over time. The next place to search for regular variability is in the structure of the coma. The nucleus-coma system is extremely complex and it is difficult to extract the coma from the nucleus. Ideally, the nucleus acts like a point source that is fuzzed out by seeing conditions, the focus of the telescope, and effects of differential refraction. The coma, which consists of gas and dust surrounding the nucleus, is expected to fall off as ρ^{-2}, where ρ is the apparent distance from the center of the nucleus. The density of the gas and dust in the coma follow the standard r^{-2}. However, because the object is observed in two dimensions, the projected column density goes as r^{-1}. Comets typically reveal behavior that falls off steeper than ρ^{-1}, but because so little is known and understood about the properties of active asteroids, the ρ^{-1} functional fit is assumed.

A Gaussian profile was created using field stars in the sidereal images. The Gaussian profiles for each of the field stars were normalized to the area under the curve and averaged together to form an ideal Gaussian profile to represent the seeing and focus conditions at that time. The FWHM seeing vector that was created in Section 5.3 was normalized to the FWHM of the ideal Gaussian profile created from the sidereal images. The vector was then applied to the Gaussian profile for each mini stacked image to account for seeing and focus conditions.

The idealized Gaussian profiles were subtracted from the 90° wedges in each of the mini stacks, where the radial wedge was mirrored to create a full profile. With the Gaussian profile removed, the remaining information should represent the coma of P/2013 P5 (Figure 18). The

residual, or coma, of each wedge was plotted for all five mini stacks (Figure 19). A similar procedure was conducted here to track the deviation of the coma as with the flux in the radial profiles (Table 5). Figure 20 shows the same five grids, each representing a stacked image. The different colored squares represent the different 90° wedges within a stack. Instead of tracking flux, the standard deviation was calculated for the absolute value of each coma profile and ranked 1:4 from largest to smallest. The resulting rankings are shows in the figure. Again, while there is variation in the structure of the coma with time and position, there is no observable pattern to the variability.

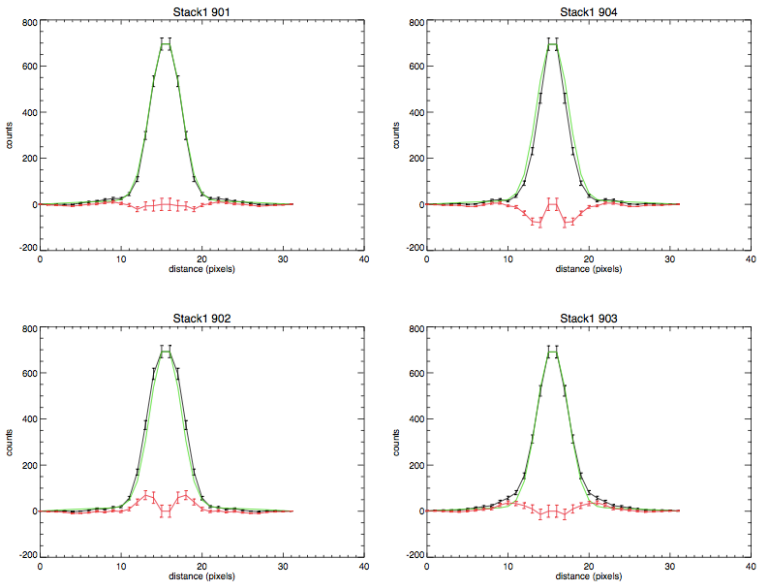

Figure 18: 90° wedges from Stack 1 (black). The ideal Gaussian profile (green) and the residual (red) are also shown.

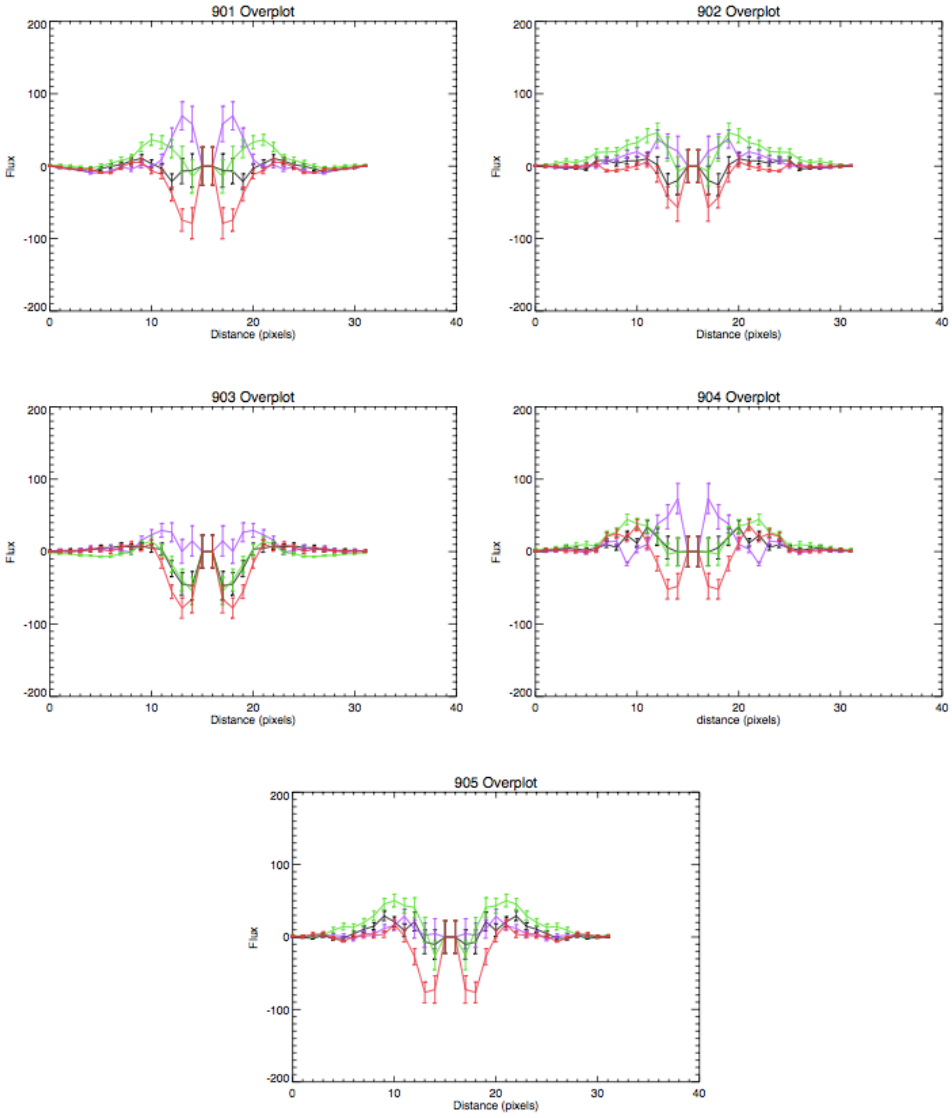

Figure 19: Residual profiles for each 90° wedge for each mini stack. The residual profile goes from the center of P/2013 P5 to the edge of the array, 3.34".

Table 5: The standard deviation of each residual after the Gaussian profile was subtracted from the 90° wedge in each mini-stack.

Wedge #	Standard Deviation
1901	7.16
1902	24.46
1903	14.25
1904	26.27
2901	9.77
2902	11.97
2903	15.90
2904	17.37
3901	17.84
3902	10.45
3903	17.13
3904	28.35
4901	9.72
4902	22.54
4903	15.33
4904	23.34
5901	11.13
5902	7.87
5903	20.71
5904	26.97

Figure 20: Change ranked from 1:4 using standard deviation in the 90° wedge. Largest Deviation=1, Smallest Deviation=4.

7. CONCLUSIONS

Photometry and morphological changes in structure and brightness of the coma-nucleus system of P/2013 P5 were investigated to search for signs of rapid rotation. Conclusions regarding the rotational properties of P/2013 P5 determined from DCT observations are as follows:

1. At an apparent magnitude of V=22.5 magnitude, we found no significant variability in the light curve at the level of 0.15 magnitudes.

2. The total flux in the coma-nucleus system is seen to vary at the level of 10% that is qualitatively inconsistent with seeing changes throughout the night.

3. Radial profiles of the 90° wedges for each mini stack further support the observed changes in total flux within the coma-nucleus system of P/2013 P5. The variation of each wedge from the mean flux per wedge is at the level of 11%.

4. Plots of the coma also reveal changes with time. The level in variation of the coma for each wedge from the mean deviation per wedge is at the level of 44%.

8. FUTURE WORK

We reached a null result with the data analysis that we have performed thus far. However, there are still future directions to pursue. The procedure used above only altered the time variable and did not account for the location of features within the nucleus-coma system. The following things can be done to further investigate morphology changes:

1. Break mini stack into individual images and plot total flux versus time for first 90° wedge. (What is the scale of the variance? How does this fit with variance in the flux versus time plot of stacks?)
2. Look at smaller wedges. (45°, 15°)
3. Look at smaller stacks. (10 mini stacks of 3 images)
4. Look at different wedge positions. (90° wedge starting at 15° instead of 0°)
5. Characterize the extinction. (For each image calculate total flux in the field stars and apply correction factor to account for extinction changes in flux of asteroid.)
6. Perform wedge procedure on 2006 BZ253. (These objects should not have a coma, so I could also use the data to form my idealized Gaussian profile.)
7. Use a well-written program to search for faint coma, tail, and any morphological changes (Sonnett et al., 2013).

If these methods still yield a null result, we can return to photometry and work to fine tune the aperture radii for our optimal aperture photometry procedure by changing aperture size by 10% or 20% and investigating the effects of these changes on the sensitivity of the light curve. We can also use elliptical apertures for trailed field stars in the asteroid-rate tracked images to improve accuracy. If this still does not result in a conclusion, we could re-observe P/2013 P5 the next time it is available to look for any signs of ongoing activity.

ACKNOWLEDMENTS

This work was supported and made possible by Lowell Observatory and the Northern Arizona University Research Experience for Undergraduates program. I would like to thank Kathy Eastwood and David Trilling for organizing and running the NAU REU program and Nicholas Moskovitz and Stephen Levine for all their support, guidance, and positive encouragement throughout the entire program.

REFERENCES

Agarwal, J., Jewitt, D., & Weaver, H. 2013, ApJ, 769, 46

Bottke, W.F., Vokrouhlick'y, D., Rubincam, D.P., & Nesvorn'y, D. 2006, AREPS, 34, 157

Consolmagno, G., Britt, D., & Macke, R. 2008, ChEG, 68, 1

Dunn, T. L., Burbine, T. H., Bottke, W. F., & Clark, J. P. 2013, Icar, 222, 273

Gumley, L.E. Practical IDL Programming: Creating Effective Data Analysis and Visualization Applications. San Diego: Morgan Kaufmann, 2002. Print.

Harris, W.E. *Stellar Photometry Using IRAF}. McMaster University Physics and Astronomy*. Sept. 2008.

Hartmann, W.K., Tholen, D.J., & Cruikshank, D.P. 1987, Icarus, 69, 33

Howell, S.B. "CCD Imaging." *Handbook of CCD Astronomy*.

Cambridge, U.K.: Cambridge UP, 2000. 47-74. Print.

Howell, S.B. "Photometry and Astrometry." *Handbook of CCD Astronomy*.

Cambridge, U.K.: Cambridge UP, 2000. 75-99. Print.

Hsieh, H. H., & Jewitt, D. 2006, Science, 312, 561

Hsieh, H.H., Jewitt, D.C., & Fern'andez, Y.R. 2004, AJ, 127, 2997

Jewitt, D. 2012, AJ, 143, 66

Jewitt, D.C., Agarwal, J., Weaver, H., Mutchler, M., & Larson, S. 2013, ApL, 778

Kryszczynska, A. 2013, A&A, 551, A102

Marzari, F., Rossi, A., & Scheeres, D. J. 2011, Icar, 214, 622

Masiero, J. R., Mainzer, A. K., Bauer, J. M., et al. 2013, ApJ, 770, 7

Massey, P. "A User's Guide to CCD Reductions with IRAF." *IRAF NOAO*., 15 Feb. 1997.

Nesvorn'y, D., Morbidelli, A., Vokrouhlick'y, D., Bottke, W. F., & Broz, M. 2002, Icar, 157, 155

Sanchez, D. P., & Scheeres, D. J. 2012, Icar, 218, 876

Scheeres, D. 2007, Icar., 189, 370

Walsh, K.J., Richardson, D.C., & Michel, P. 2008, Natur, 454, 188

Table 2: Summary of Observations.

UT Time	Exposure Time (s)	Airmass	Tracking	Filter
2:09:08	180.0	1.250	sidereal	SDSS-r
2:15:59	180.0	1.250	sidereal	SDSS-r
2:30:39	180.0	1.250	sidereal	SDSS-r
2:40:26	300.0	1.260	sidereal	SDSS-r
2:58:42	300.0	1.270	asteroid-rate	SDSS-r
3:07:36	300.0	1.280	asteroid-rate	SDSS-r
3:12:59	300.0	1.290	asteroid-rate	SDSS-r
3:18:23	300.0	1.300	asteroid-rate	SDSS-r
3:23:47	300.0	1.310	asteroid-rate	SDSS-r
3:29:11	300.0	1.320	asteroid-rate	SDSS-r
3:34:34	300.0	1.330	asteroid-rate	SDSS-r
3:39:58	300.0	1.350	asteroid-rate	SDSS-r
3:45:22	300.0	1.360	asteroid-rate	SDSS-r
3:50:46	300.0	1.370	asteroid-rate	SDSS-r
3:56:09	300.0	1.390	asteroid-rate	SDSS-r
4:18:20	300.0	1.470	asteroid-rate	SDSS-r
4:23:44	300.0	1.490	asteroid-rate	SDSS-r
4:29:08	300.0	1.520	asteroid-rate	SDSS-r
4:34:32	300.0	1.540	asteroid-rate	SDSS-r
4:39:55	300.0	1.570	asteroid-rate	SDSS-r
4:45:19	300.0	1.600	asteroid-rate	SDSS-r
4:50:43	300.0	1.630	asteroid-rate	SDSS-r
4:57:00	300.0	1.670	asteroid-rate	SDSS-r
5:02:23	300.0	1.710	asteroid-rate	SDSS-r
5:07:47	300.0	1.750	asteroid-rate	SDSS-r
5:13:11	300.0	1.790	asteroid-rate	SDSS-r
5:18:35	300.0	1.840	asteroid-rate	SDSS-r
5:23:58	300.0	1.890	asteroid-rate	SDSS-r
5:29:22	300.0	1.940	asteroid-rate	SDSS-r
5:34:46	300.0	2.000	asteroid-rate	SDSS-r
5:40:10	300.0	2.060	asteroid-rate	SDSS-r
5:45:33	300.0	2.130	asteroid-rate	SDSS-r
5:57:18	300.0	2.280	asteroid-rate	SDSS-r
6:01:41	300.0	2.370	asteroid-rate	SDSS-r
6:07:05	300.0	2.460	asteroid-rate	SDSS-r

Table 3: The seeing quantified in reference to both time and airmass.

UT Time	Airmass	Optimized Aperture Radius
2:09:08	1.25	2.41606
2:15:59	1.25	2.5187
2:30:39	1.25	2.59601
2:40:26	1.26	2.82138
2:58:42	1.27	2.56028
3:07:36	1.28	2.67632
3:12:59	1.29	2.69327
3:18:23	1.30	2.75841
3:23:47	1.30	2.62533
3:29:11	1.32	2.7095
3:34:34	1.33	2.90044
3:39:58	1.35	2.8589
3:45:22	1.36	3.17944
3:50:46	1.37	2.90161
3:56:09	1.39	3.04542
4:18:20	1.47	3.11574
4:23:44	1.49	3.02146
4:29:08	1.52	3.04067
4:34:32	1.54	3.135
4:39:55	1.57	3.09803
4:45:19	1.60	2.99018
4:50:43	1.63	2.97049
4:57:00	1.67	3.03128
5:02:23	1.71	2.9834
5:07:47	1.75	2.97043
5:13:11	1.79	3
5:18:35	1.84	3.31264
5:23:58	1.89	3.09136
5:29:22	1.94	3.12041
5:34:46	2.00	3.11503
5:40:10	2.06	3.26017
5:45:33	2.13	3.57816
5:57:18	2.28	3.34157
6:01:41	2.37	3.64381
6:07:05	2.46	3.67929